Supporting Information

Palva et al. 10.1073/pnas.0913113107

SI Text

Filtering. The time series of each channel, $y_j(t)$, of the single-trial MEEG, $Y(t)$, with n_c channels $j = 1...n_c$ (here, $n_c = 366$), was filtered into 36 frequency bands with a bank of Morlet wavelets $h(t,f)$ that had roughly log-linearly spaced center frequencies, f ($f = 3...90$ Hz) (Fig. S1*C*). The complex-filtered signal $y_F(t,f)$ was given by $y_F(t,f) = y(t) * h(t,f)$, where * denotes convolution and $h(t,f) = A\exp(-t^2/2\sigma_t^2)\exp(2i\pi ft)$. The time domain SD, σ_t, of the wavelet is $\sigma_t = m/2\pi f$, where the parameter m ($m = 5$) defines the compromise between time and frequency resolution.

Forward and Inverse Modeling. The FreeSurfer image analysis suite, which is documented and freely available online (http://surfer.nmr.mgh.harvard.edu/), was used for automatic volumetric segmentation of the MRI data and for the reconstruction, flattening, and automatic labeling and parcellation of cortical surfaces (1–7) (Fig. S1*D*). The MNE software (http://www.nmr.mgh.harvard.edu/martinos/userInfo/data/sofMNE.php) was used for creating three-layer boundary element conductivity models and cortically constrained source models for forward and inverse modeling (Fig. S1*E*). The MNE was also used for MEEG-MRI colocalization and for the preparation of the forward and inverse operators (8–11) (Fig. S1 *E* and *F*). Individual subjects' source models were based on tessellated cortical surfaces on which the dipoles were normal to the surface and had a 7-mm dipole-to-dipole separation. The source models had a total of $n_d = 6{,}000$–$8{,}500$ dipoles (source-model vertices) in the two cerebral hemispheres.

MEEG sensor signals, Y, are linearly related to the current strengths of the n_d source dipoles, $X = [x_k]$, $k = 1...n_d$, such that $Y(t) = \Gamma X(t) + N(t)$, where N denotes noise and Γ is the lead field matrix (i.e., the forward operator that relates the source dipole strengths to the sensor level data jointly acquired by MEG planar gradiometers, MEG magnetometers, and EEG electrodes). We obtained $X(t)$ from measured $Y(t)$ by using a minimum norm estimator (8), such that $X(t) = MY(t) = R\Gamma^T(\Gamma R\Gamma^T + \lambda^2\chi)^{-1}Y(t)$, where M is the inverse operator, λ^2 is a regularization parameter, R is the source covariance matrix, and χ is the noise covariance matrix. We used $\lambda^2 = 0.05$ and a multiple of the identity matrix as R. The inverse operator, M, for each wavelet frequency was prepared with noise covariance matrices computed across the real parts of filtered single-trial prestimulus baseline windows (Fig. S1*G*). Frequency-specific complex inverse solutions, $X_F = [x_{F,k}]$, were obtained from the inverse estimates of the real ($Y_{F,RE}$) and imaginary ($Y_{F,IM}$) parts of the filtered MEEG data, Y_F, such that $X_F = M_F\, Y_{F,RE}(t) + i\, M\, Y_{F,IM}(t)$, where i is the imaginary unit (Fig. S1*H*).

Surface Parcellation. Two parcellations of the source model were used in the quantification of interareal phase synchrony. Here, the term "parcellation" means a set of patches, each of which defines a set of source model vertices. The first one, a cluster parcellation, P_{CL}, with 365 patches, was obtained with a mean linkage clustering algorithm that yielded maximally independent cortical patches in individual anatomy and was used to compute the within-subject phase synchrony estimates. The second one, an anatomical landmark parcellation, P_{AN}, was based on automatic cortical labeling (5) and was used for group statistics and visualization.

Clustering parcellation. Source-space interaction mapping would be directly achievable through a computation of source model vertex-by-vertex ($n_d \times n_d$) phase synchrony matrices, but they would be highly redundant and computationally cumbersome. Hence, after the inverse modeling and before the phase synchrony estimation, we collapsed the 6,000–8,500 time series of the source vertices into 365 time series of the cortical patches (Fig. S1*I*). The collapsed inverse solution, $X_{F,P} = [x_{F,P,l}]$, $l = 1...n_p$, is given by $X_{F,P} = \Pi(X_F, P)$, where Π is a collapse operator; P is the parcellation, $P = [p_l]$; and n_p is the number of patches, p_l, in P. We defined Π so that the complex time series of a patch's phase is given by $x_{F,P,l}(t,f) = \rho_l/|\rho_l|$, where $\rho_l = q_l^{-1}\,\Sigma_u\, x_{F,u}$, $u = 1...q_l$ are the indices of the source vertices in patch p_l and q_l is the number of source vertices in that patch. Within-subject phase synchrony analysis was obtained with a P_{CL} that maximized the separability of cortical sources in individual anatomy. The parcellation was based on an estimate of artifactual synchrony that was obtained by simulating white noise in each source model vertex, forward modeling it to achieve a virtual MEEG recording, Y_v; filtering and inverse modeling the data to obtain $X_{F,v}$; and then estimating from $X_{F,v}$ across 5,000 independent samples the complete pair-wise source vertex-by-vertex phase synchrony matrix, I_v (Fig. S1*J*). This "artefact synchrony matrix" thus quantifies the artifactual correlations caused by the MEEG measurement as well as those arising in the inverse modeling. A total of 365 cortical patches were obtained with mean linkage clustering of I_v, such that vertices, or clusters of vertices, with the strongest pair-wise phase synchrony were clustered together. For each clustering step, parcellation was applied to the 5,000-sample $X_{F,v}$ and the artifact synchrony matrix was recomputed. This process was iterated until 365 source clusters remained (Fig. S1*K*).

Neuroanatomical parcellation. The FreeSurfer software parcellates and labels the cortical surface into 156 patches in two hemispheres based on gyral and sulcal structure and neuroanatomical convention (see above; Fig. S1*D*). These patches were the basis of our group level statistics and visualization. To exclude the possibility that the size variability of these patch-biased network analyses, we further split the largest and merged the smallest patches to obtain an anatomical parcellation, P_{AN} (Fig. S1*L*). We first iteratively searched for patches that had the largest size in the subject population and split them along the axis (anterior-posterior, lateral-medial, ventral-dorsal) that had the largest mean variance (Fig. S1*L*). This procedure was used to obtain a total of 240 patches in the two hemispheres with split directions that were identical for every subject. We then iteratively merged smaller patches with their neighbors to obtain a collection of 106 patches in two hemispheres, with 63 ± 23 source space vertices per patch (mean ± SD). P_{AN} thus retains the individual anatomical accuracy and yet provides a common basis for statistics across subjects.

Estimation of Interareal Interactions in Source Space. We used the collapsed inverse estimates, $[X_{F,P,r}(t,f)]$, of single trials, r ($r = 2...n_t$), for mapping cortex-wide interareal interactions, such that $I = S([X_{F,P,r}])$, where I $[I = I(t,f)]$ is an $n_p \times n_p$-sized matrix of interaction strengths, S is the interaction operator, and n_t denotes the total number of trials in the experimental condition (Fig. S1*M*). In this study, neuronal interactions were indexed by pair-wise phase synchrony of each cortical patch with every other patch. Two signals are said to be phase-synchronized if their phase difference distribution is nonrandom. Phase synchrony between a pair of patches, p_a and p_b, was quantified across trials by using a *PLV*, $PLV(t,f)$, that was given by $PLV = (n_t - 1)^{-1}|\Sigma_r(x_{F,P,a,r}\, x^*_{F,P,b,r})|$, where Σ_r denotes the sum across trials and x^* is the complex conjugate of x. The interaction matrix, I, for a given

parcellation, P, is then obtained by computing PLV for each pair (a, b), $a = 1...n_p$, $b = 1...n_p$, which is also conveniently given by the outer product $I = (n_t-1)^{-1}|\Sigma_r(X_{F,P,r} \otimes X^*_{F,P,r})|$. An estimate, I_{evk}, of phase synchrony artifactually caused by signal components that were phase-locked to the sample stimulus, "evoked synchrony," was estimated as for I above but by using a trial-shifted PLV that was given by $PLV_{evk} = (n_t-1)^{-1}|\Sigma\,(x_{F,P,a,r}\, x^*_{F,P,b,r-1})|$. I and I_{evk} were obtained for each subject, condition, time window (width = 300 ms, overlap = 145 ms), and wavelet center frequency (36 frequencies from 3 to 90 Hz). One wavelet with a center frequency at around 50 Hz was excluded from the analyses because of putative mains interference.

Group Statistics. In addition to the estimates of evoked phase synchrony, I_{evk}, we obtained estimates of the average level of phase synchrony in the presample-stimulus baseline, I_{bl}, and used these to remove artifactual and task-irrelevant components from the individual subject's interaction strength matrices, $I(t,f)$. This correction was given by $I_{corr}(t,f) = I(t,f) - \max[I_{bl}(f), I_{evk}(t,f)]$, where $I_{bl}(f)$ is the mean of $I(t,f)$ across the baseline period (time windows with centers from −450 to −140 ms) and the max-operation is the maximum of $I_{bl}(f)$ or $I_{evk}(t,f)$ separately for each $PLV(t,f)$. Thus, the $I_{corr}(t,f)$ values were biased neither by baseline nor by stimulus-locked activity. The baseline correction also intrinsically removes possible artifactual pair-wise synchrony arising from the MEEG recording or inverse modeling. Individual subjects' corrected interaction matrices, $I_{corr}(t,f)$, which were obtained in P_{CL}, were then morphed by patch area-weighted averaging into those individuals' P_{AN}s to obtain $I_{AN,corr}(t,f)$ for usage in group statistics.

The statistical interaction matrix, $I_S(t,f)$ (Fig. S1*N*), contains the significance (P value) of each pair-wise interaction in each condition. We obtained $I_S(t,f)$ from the $I_{AN,corr}(t,f)$ of all subjects by applying a statistical test separately for each pair-wise PLV for each t and f. In the average condition, $I_{AN,corr}(t,f)$ values were tested against a null hypothesis of $PLV \leq 0$ using the Wilcoxon signed rank test. For each subject, the $I_{AN,corr}(t,f)$ was obtained by averaging the six $I_{corr}(t,f)$ values that were computed separately with an equal number of trials corresponding to L_M (L_M = 1, 2, 3, 4, 5, and 6). In the load condition, $I_{AN,corr}(t,f)$ values were obtained separately and with an equal number of trials for each L_M = 1, 2, 3, 4, 5, and 6, and were then tested across subjects using the Spearman's rank correlation test against a null hypothesis that $PLV(L_M)$ is uncorrelated or negatively correlated with L_M. The interactions predicting individual behavioral memory capacity were identified so that we obtained the $I_{corr}(t,f)$ for each L_M = 1, 2, 3, 4, 5, and 6 and searched the k_L that gave the best least-squares fit of the capacity function $F_{cap}(L_M,g,k_L)$, where g indicates gain parameter, with $PLV(L_M)$. These best-fitting k_L values were then tested across subjects with the Spearman's rank correlation test against the null hypothesis that k_L values were uncorrelated or negatively correlated with the subjects' individual behavioral capacity k_P (see above). $F_{cap}(L_M, g,k_L)$ was obtained for each L_M (1...6) so that the value of F_{cap} increased linearly between $1 \leq L_M \leq k_L$ and remained at the maximum level from $k_L \leq L_M \leq 6$. During the least-squares fitting, g was used for scaling F_{cap}.

Graph Characterization. We used network metrics from graph theory to characterize the interaction data (12, 13) (Fig. S1*O*). In our graphs, vertices are the brain areas and the connecting edges are the interareal interactions. Binary and undirected graphs, G, were obtained from adjacency matrices A_G ($A_G = T[I_S(t,f)]$), where T denotes a threshold operator. The thresholding was carried out by first nulling elements of $I_S(t,f)$ for which $P > A$, where A is the A level. To compensate for false-positive results arising from multiple comparisons, we used the A level to indicate the proportion of false rejections of the null hypothesis and then the total number of performed tests to predict the number of false discoveries. To obtain an FDR < 0.01, we removed 99% of the number of elements predicted to be false discoveries from the remaining nonzero elements of $I_S(t,f)$ in decreasing order of p.

We used connection density, K, as the initial graph level measure of interareal connectedness (Figs. 1 and 4). K is the number of edges present in the graph (graph's size) divided by the number of all possible edges. Vertex degree, d, denotes the number of edges connected to the vertex (Fig. 1*C*). A k-core analysis was used to identify densely interconnected "core" structures (Figs. S3, S5, and S6). Vertices belonging to a k-core are identified as those that remain after removing vertices with $d < k$, along with their edges iteratively until all remaining vertices have $d \geq k$. A graph's maximum k-core number is the value of k, such that all vertices are removed with $k + 1$. The k-coreness of an individual vertex is the value of k, such that the vertex is removed with $k + 1$. We identified network hubs by using degree and betweenness centrality. Betweenness centrality, $C_{B,i}$, of vertex i is the number of shortest paths between pairs of other vertices that pass through i divided by the total number of shortest paths between pairs of other vertices. Betweenness centrality was computed with a Matlab algorithm provided in the Brain Connectivity Toolbox (http://sites.google.com/a/brain-connectivity-toolbox.net/bct/home).

To estimate the edge-wise similarity of two graphs (Fig. S2), we define the edge-wise graph similarity index, $S^E, 0 \leq S^E \leq 1$, between binary G_i and G_j, such that $S^E = |A_{G,i} \cap A_{G,j})|/|A_{G,i} \cup A_{G,j}|$. For statistics, S^E values were compared against the distribution of S^E values obtained for order- and mean degree-matched random graphs. We corroborated the edge-wise similarity data with a vertex-wise similarity metric, S^V, that was obtained with a Spearman's rank correlation coefficient and statistics of vertex degree sequences.

For merging a set of graphs $G_1...G_N$ into a matching graph, G_M, we first obtained a weighted matching adjacency matrix, $A_{G,M}$, from binary adjacency matrices $A_{G,i}$ ($i = 1...N$), with $A_{G,M} = N^{-1}\Sigma(A_{G,i})$. Elements of $A_{G,M}$ are the edge-matching indices M^E ($0 \leq M^E \leq 1$). To obtain comparable network characterizations and visualizations (Figs. S3, S5, and S6), the binary G_M values were obtained from $A_{G,M}$ by thresholding with as large a $M^E{}_{min}$ as possible that gave a $K \geq 0.1$ but so that the minimum value of $M^E{}_{min}$ was 0.1. The simplified graphs shown in Figs. 2–4 were obtained from Figs. S3, S5, and S6, as indicated in figure legends, by finding an $M^E{}_{min}$ that gave a $K \geq 0.02$. Note that the $M^E{}_{min}$ of each graph (required for achieving the constant K across graphs) is reported in the corresponding figure legend and, in itself, indexes the degree of spectral and temporal stability of the matching graph. The progressive pruning of the matching graphs by an increasing $M^E{}_{min}$ is illustrated in Fig. S8. Spectral colocalization graphs (details provided in Fig. S4) were obtained as matching graphs across the frequency bands with the addition of thresholded band-specific edge coloring at the matching graph threshold $M^E{}_{min} = 0.15$, which gave $K = 0.1$ in both the average and load conditions. As in Figs. 2 and 3, each of the three frequency bands contained four time windows and wavelet frequencies.

The graph structures reported in this study were robust against even large changes in the A level, FDR correction, and $M^E{}_{min}$. The data were also robust against moderate changes in the time window and frequency band selections.

Relation Between Amplitude Modulations and Phase Synchrony. Theoretically, changes in oscillation amplitudes may cause changes in phase synchrony. This is because an increase in the signal-to-noise ratio (SNR) enables more accurate estimates of the phase and, consequently, leads to a greater PLV with the same underlying neuronal interaction. In our data, however, several lines of evidence rule out the possibility that changes

in the SNR could cause the observed changes in long-range synchrony.

We first simulated the dependence of the *PLV* of coupled signals on the SNR and on the coupling strength (Fig. S7*A*). The simulations were based on two parametrically coupled noise processes, X and Y, with a variable magnitude of uncorrelated "measurement noise," such that $X = A + cB + sC$ and $Y = B + cA + sD$, where A, B, C, and D are independent realizations of white noise in the range from −1 to 1; c is the coupling constant; and s is the noise amplitude parameter, such that $s = \mathrm{SNR}^{-1}$. SNR is thus defined here as the amplitude of the signal divided by the amplitude of the noise. To obtain the complex time series of the phase, X and Y were Morlet wavelet-filtered to give $X_\mathrm{F} = X * h(t,f)$ and $Y_\mathrm{F} = Y * h(t,f)$ and were normalized to $X_\mathrm{F,n} = X_\mathrm{F}/|X_\mathrm{F}|$ and $Y_\mathrm{F,n} = Y_\mathrm{F}/|Y_\mathrm{F}|$, where $f = 0.1f_\mathrm{s}$ and f_s is the sampling rate. To evaluate the sensitivity of phase synchrony estimation to SNR, the expected *PLV* was estimated across the time series, such that $plv = n_\mathrm{r}^{-1}|\Sigma\ (X_\mathrm{F,n}\ Y^*_\mathrm{F,n})|$, where $n_\mathrm{r} = 10^5$ is the number of noise process samples and $PLV = n_\mathrm{s}^{-1}\Sigma\ (plv)$, where $n_\mathrm{s} = 10^5$ indicates the number of realizations of the noise processes for each value of c and s. The s parameter was varied to produce log-linear SNR spacing where $\mathrm{SNR}_{i+1} = \mathrm{SNR}_i \times 1.3$. Fig. S7*A* shows that the *PLV* is dependent both on the strength of coupling and on the SNR. The constant change in SNR makes it now easy to plot the relative change in the *PLV* for each step in SNR by defining relative change as $(PLV_{i+1} - PLV_i)/PLV_i$ (Fig. S7*B*). Fig. S7*B* shows that at SNR > 1, the relative increase in *PLV* for a constant relative improvement in SNR (here, 1.3) decays rapidly, such that at higher SNRs, a change in SNR has only a minor effect on the estimated *PLV*. Fig. S7*B* also shows that at SNR < 1, the changes in *PLV* caused by modulations of SNR are large and dependent on the true (and underestimated, compare with Fig. S7*A*) coupling strength.

By mapping with simulations the *PLV* as a function of both c and SNR and by estimating the *PLV*, SNR, and amplitude levels from recorded data, it is possible to predict the effect that an amplitude change would have on the *PLV* and then compare this prediction with the recorded change in *PLV*. We estimated the average apparent SNR of MEG gradiometers and magnetometers for each subject in the frequency bands of interest (α, β, and γ) by comparing the recorded data with empty-room MEG recordings that were performed before or after each recording session. The apparent SNR (aSNR) was estimated from the averaged wavelet amplitudes, such that $\mathrm{aSNR} = n_\mathrm{c,MEG}^{-1}\Sigma_\mathrm{j}\ [(A_\mathrm{b,j} - A_\mathrm{n,j})/A_\mathrm{n,j}]$, where $n_\mathrm{c,MEG}$ is the number of MEG channels ($n = 306$), $A_\mathrm{b,j}$ indicates the average amplitude of the experimental data (neuronal activity + environmental noise), and $A_\mathrm{n,j}$ indicates the average amplitude of empty room noise for MEG channel j. The mean aSNR values were α-band = 3.42 ± 1.67 (mean ± SD), β-band = 1.55 ± 0.76, and γ-band = 0.75 ± 0.46. It is important to note that because amplitude is a nonlinear metric, the relation between aSNR and the true SNR is a nonlinear function [i.e., in the simulations above, the (true) SNR ratio was defined to be the ratio of amplitudes of signal and noise, but the (experimentally quantifiable) amplitude of the composite signal is less than the sum of the amplitudes of signal and noise because it is the real values, and not the amplitudes of the signal and noise, that are summed]. The function linking the aSNR and SNR was estimated numerically by creating $2{\cdot}10^7$ sample white noise signal, noise, and signal plus noise time series as above with a log-linearly increasing SNR. Now, the aSNR as a function of SNR is given by $\mathrm{aSNR} = (A_\mathrm{S+N} - A_\mathrm{N})/A_\mathrm{N}$, where $A_\mathrm{S+N}$ is the average amplitude of the wavelet-filtered signal plus noise time series and A_N is the average amplitude of the wavelet-filtered noise time series (Fig. S7*C*).

We used grand average baseline and VWM retention period amplitude data, the grand average aSNR estimates, and the simulation-derived model to predict the change in *PLV* that would be caused by the recorded change in amplitude. We made the approximation that after inverse modeling, the grand average aSNR corresponds to the grand average band amplitude, A, across the cortical surface. The patch-wise aSNR_l was then obtained from the absolute patch amplitude A_l by scaling: $\mathrm{aSNR}_l = \mathrm{aSNR} \times \mathrm{A}_l/A$. Thus, grand average amplitudes of average condition baseline and the one-object condition retention period were used to estimate the initial patchwise aSNR, and the grand average amplitudes of the average and six-object condition retention periods gave the amplitude change-modulated patchwise aSNR. The observed and SNR change-predicted *PLV* values corresponding to these "initial" and "modulated" conditions were obtained for those pairs of cortical patches in which the recorded *PLV*s were statistically significant ($P < 0.01$, uncorrected). The choice of the A level, however, did not have a noticeable influence on the conclusions drawn hereafter. The SNR change-related change in each interareal *PLV* was predicted by first obtaining the initial condition *PLV* and evaluating the average initial and modulated aSNRs of the corresponding pair of cortical patches. The true initial and modulated SNRs were obtained from the aSNRs by interpolating the data in Fig. S7*C*. The modulated condition *PLV* was then given by first interpolating the data in Fig. S7*A* at the initial *PLV* and SNR to find the c corresponding to the initial *PLV* and then using this c and the modulated SNR to predict the modulated *PLV*.

In the average condition, the modulations of amplitude, *PLV*, and SNR were compared between the averaged baseline values and the four retention period time windows for each of the four wavelets in each frequency band. The load condition was approximated by a direct time frequency window-by-time frequency window comparison of the retention periods of the six-object and one-object memory load conditions to allow a quantitative evaluation of the *PLV* amplitude relation therein. Hence, in both the average and six-object vs. one-object conditions, we obtained data from 16 graphs per frequency band.

In the average condition (Fig. S7*D*), the *PLV* changes predicted by the change in amplitude from baseline to the retention period (Fig. S7*D*, red dots) clearly did not explain the experimentally observed *PLV* changes (Fig. S7*D*, black dots) in the α-, β-, or γ-band. This was not brought about by the aSNR scaling, because a nonscaled aSNR did not predict larger *PLV* changes (Fig. S7*D*, blue dots). Overall, the predicted *PLV* changes were much smaller in magnitude than the observed *PLV* changes. Moreover, because the retention period amplitudes were largely suppressed below the baseline level, the predicted *PLV* values were opposite to the recorded *PLV* changes in most cases. It is thus important to note that a widespread cortical amplitude suppression is associated with an increase in interareal phase synchrony (numerical details provided in Fig. S7*F*) in this study. Hence, the common interpretation of an amplitude suppression to imply "desynchronization" might not be accurate for spatial scales larger than those that can be separated with source modeling.

With the six-object vs. one-object condition, we addressed whether there was a load-dependent increase in the retention period amplitude that could predict the load-dependent increase in phase synchrony. Indeed, the data revealed both an amplitude and a *PLV* increase from the one- to the six-object memory load and that the *PLV* was weakly correlated with amplitude (Fig. S7*E*, numerical details provided in Fig. S7*F*). The enhanced *PLV*, however, did not arise from the amplitude increase-caused enhancement in the SNR, because the predicted *PLV* values were saliently smaller than the observed values. It is also clear that a considerable proportion of the strengthened *PLV* values are associated with negative or close-to-zero amplitude modulations (Fig. S7*E*). In the α-band, where the load-condition effects were the strongest, the mean relative change in *PLV* [11.3 ± 4.6% (mean ± SD)] was more than 18 times greater than the predicted SNR-caused change in *PLV* (0.6 ± 0.5%). We also

estimated the fraction of *PLV* values that was predicted at an accuracy of 30% by the SNR change. The percentages of accepted predictions were very small, ranging from 0 to 1.82% (Fig. S7*F*). Furthermore, we evaluated the effects that a gross misestimation of the aSNR could have. Even an aSNR as low as 0.5 did not dramatically increase the percentage of accepted predictions (range: 1.35–5.39%). Hence, we conclude that the both the average and six-object vs. one-object condition data in Fig. S7 strongly suggest that the observed changes in phase synchrony were not caused by SNR-related effects resulting from amplitude modulations.

The MEEG signal amplitude is strongly dependent on local neuronal synchronization. The six-object vs. one-object condition data thus lead to a hypothesis that the load-dependent amplitude increase, in fact, could be caused by the underlying strengthening of phase synchrony. This is plausible in light of the highly clustered structure of the frontoparietal α-band network, which has a large amount of short/medium-range connections. The relative mean strengthening of phase synchrony was also roughly two times greater in magnitude than the relative amplitude effect. Future studies could exploit forward modeling to disentangle the interactions and separability of phase synchrony and amplitude metrics, which are widely used in human MEG and EEG studies.

1. Dale AM, Fischl B, Sereno MI (1999) Cortical surface-based analysis. I. Segmentation and surface reconstruction. *NeuroImage* 9:179–194.
2. Fischl B, Sereno MI, Dale AM (1999) Cortical surface-based analysis. II: Inflation, flattening, and a surface-based coordinate system. *NeuroImage* 9:195–207.
3. Desikan RS, et al. (2006) An automated labeling system for subdividing the human cerebral cortex on MRI scans into gyral based regions of interest. *NeuroImage* 31:968–980.
4. Fischl B, et al. (2004) Automatically parcellating the human cerebral cortex. *Cereb Cortex* 14:11–22.
5. Fischl B, et al. (2002) Whole brain segmentation: Automated labeling of neuroanatomical structures in the human brain. *Neuron* 33:341–355.
6. Ségonne F, et al. (2004) A hybrid approach to the skull stripping problem in MRI. *NeuroImage* 22:1060–1075.
7. Fischl B, Liu A, Dale AM (2001) Automated manifold surgery: Constructing geometrically accurate and topologically correct models of the human cerebral cortex. *IEEE Trans Med Imaging* 20:70–80.
8. Hämäläinen MS, Sarvas J (1989) Realistic conductivity geometry model of the human head for interpretation of neuromagnetic data. *IEEE Trans Biomed Eng* 36:165–171.
9. Hämäläinen MS, Ilmoniemi RJ (1994) Interpreting magnetic fields of the brain: Minimum norm estimates. *Med Biol Eng Comput* 32:35–42.
10. Mosher JC, Leahy RM, Lewis PS (1999) EEG and MEG: Forward solutions for inverse methods. *IEEE Trans Biomed Eng* 46:245–259.
11. Lin FH, Belliveau JW, Dale AM, Hämäläinen MS (2006) Distributed current estimates using cortical orientation constraints. *Hum Brain Mapp* 27:1–13.
12. Bullmore E, Sporns O (2009) Complex brain networks: Graph theoretical analysis of structural and functional systems. *Nat Rev Neurosci* 10:186–198.
13. Rubinov M, Sporns O (2009) Complex network measures of brain connectivity: Uses and interpretations. *NeuroImage,* doi:10.1016/j.neuroimage.2009.10.003.

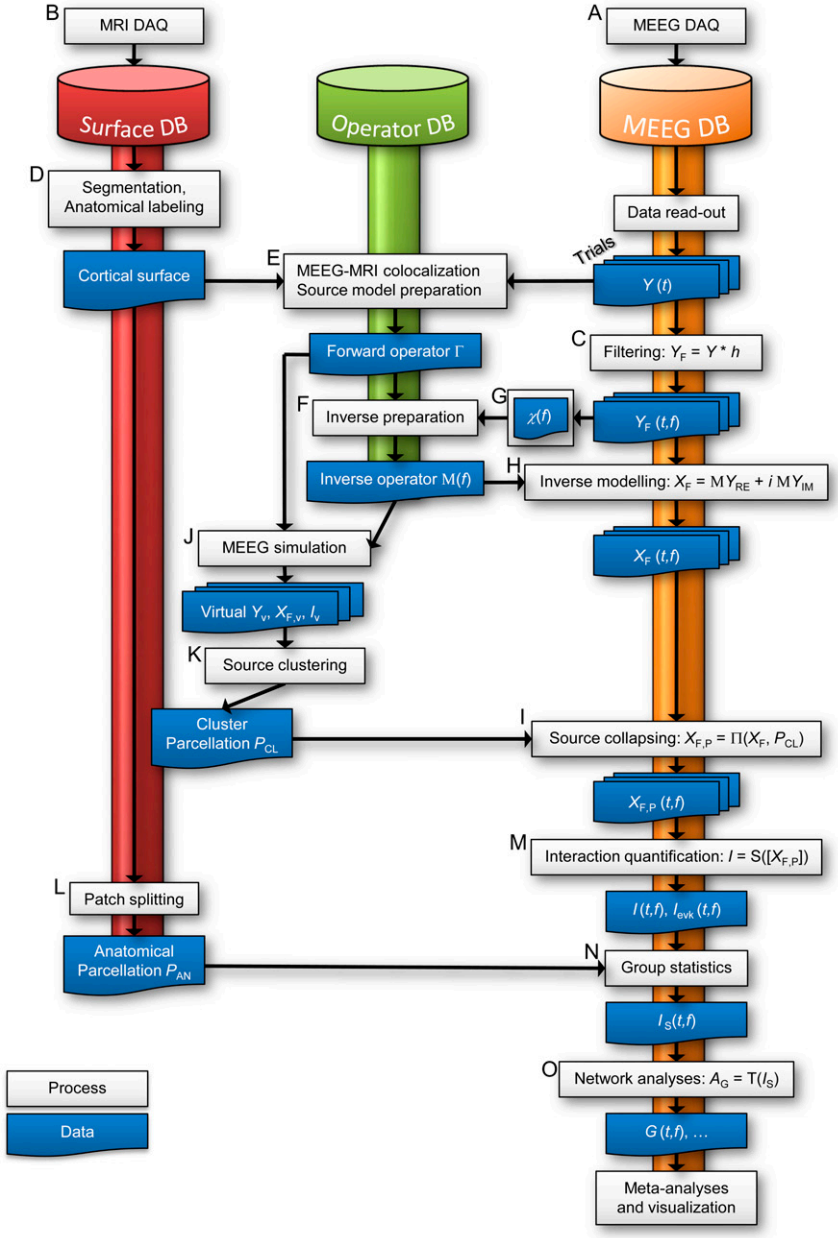

Fig. S1. Workflow and variables for cerebral interaction mapping. Details are provided in *SI Text*.

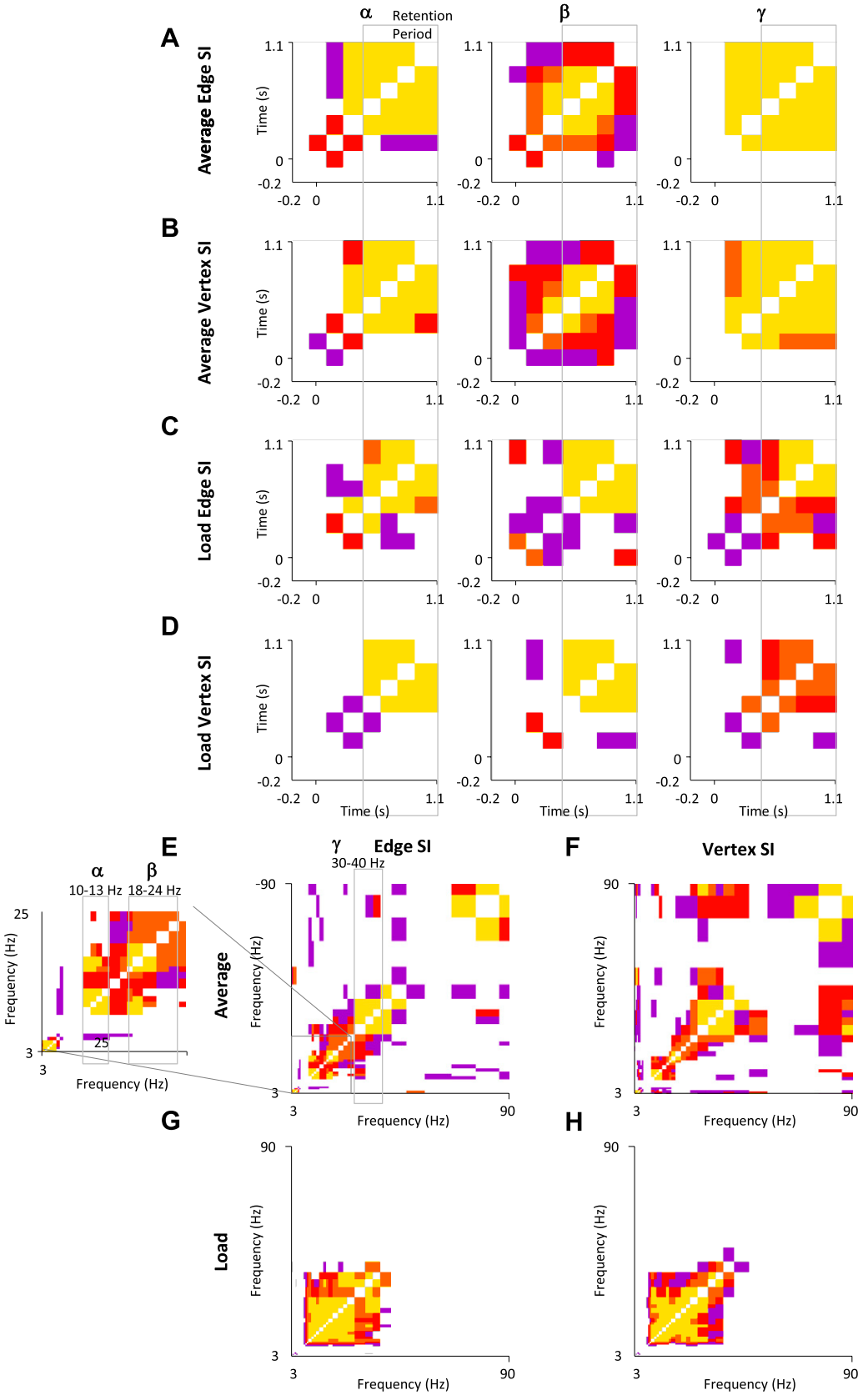

Fig. S2. Edge- and vertex-wise graph similarity estimates indicate that network structures in α-, β-, and γ-frequency bands are sustained throughout the VWM retention period. (*A*) Average condition edge similarity index (SI) statistics in all time windows (x and y axes) for α-, β-, and γ-frequency bands. The colors indicate the number of graphs in the specific frequency band that were significantly similar for each time window-time window pair ($P < 0.01$, Bonferroni-corrected with the number of graphs in the frequency bands; colors: yellow, 4; orange, 3; red, 2; purple, 1) (4). To qualify as "significantly similar," we required that a minimum of two of four graphs (corresponding to four wavelet center frequencies in each frequency band) were significantly similar ($P < 0.01$, cor-

Legend continued on following page

rected) throughout the retention period (four time windows). The gray rectangle indicates the four time windows denoted as the retention period in this study. (*B*) Average condition vertex similarity statistics among time windows. Frequency bands and colors are as in *A*. Load condition edge (*C*) and vertex similarity (*D*) statistics. Frequency bands and colors are as in *A*. Taken together, the data in *A–D* indicate that α-, β-, and γ-frequency band networks are significantly similar throughout the VWM retention period, which we define to be the last four time windows with centers from 480 to 945 ms. (*E*) Average condition edge similarity statistics among all wavelet frequencies (x and y axes) across the retention period. The colors indicate the number of graphs that were significantly similar for each frequency-frequency pair ($P < 0.01$, Bonferroni-corrected with the number of graphs in the retention period; colors: yellow, 4; orange, 3; red, 2; purple, 1) (4). Gray squares indicate the α-, β-, and γ-frequency bands. (*F*) Average condition vertex similarity statistics among wavelet frequencies. Colors are as in *E*. Load condition edge (*G*) and vertex similarity (*H*) statistics are as in *E*. The data in *E* and *F* show that in the average condition, graphs within α-, β-, and γ-bands were strongly self-similar, but there was less overlap across frequency bands. In the load condition (*G* and *H*), on the other hand, graphs were significantly similar almost throughout the α-, β-, and γ- (10–40 Hz) ranges.

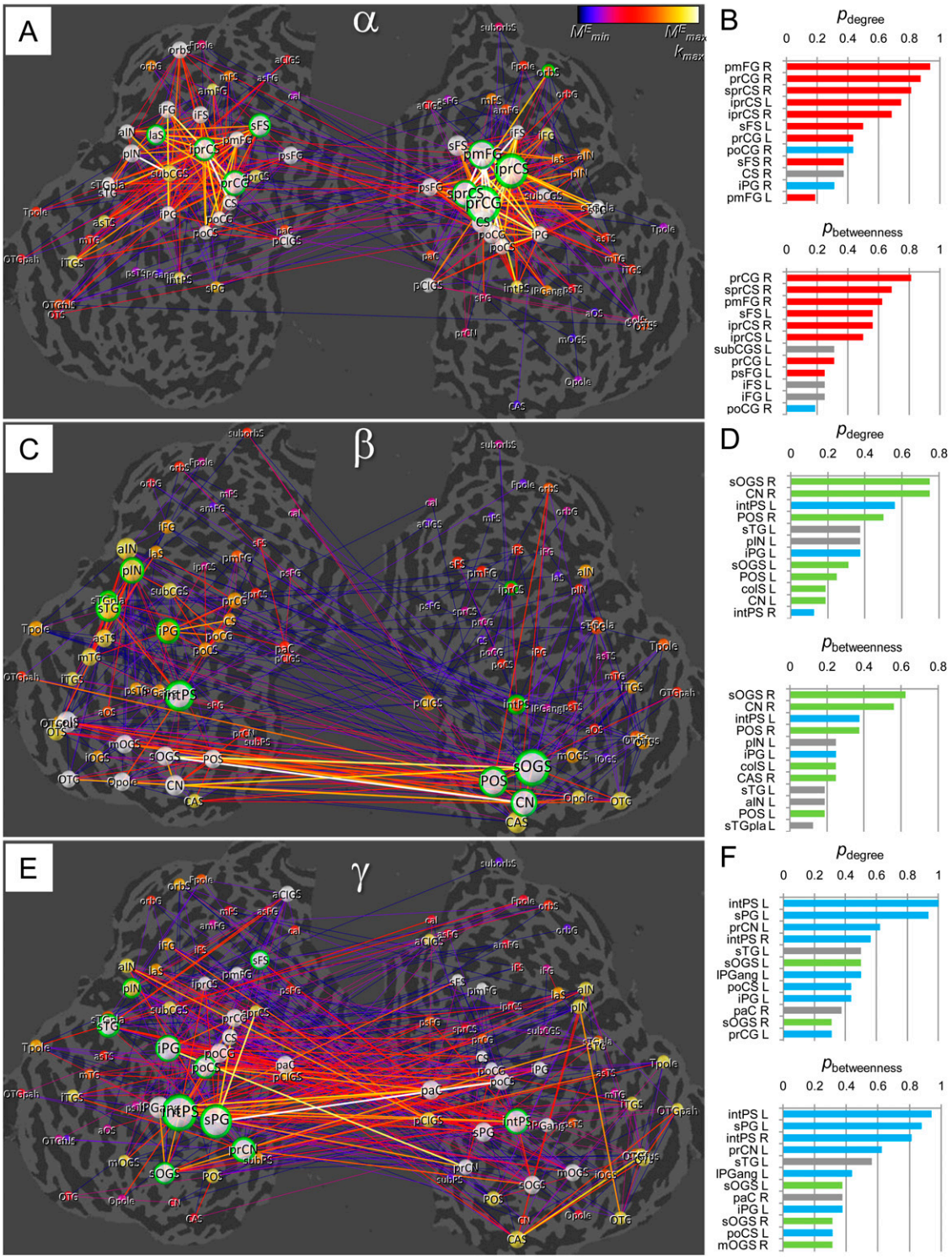

Fig. S3. Complete average condition matching graphs and hub classification for Fig. 2. Each matching graph was obtained from four wavelet frequencies and four retention period time windows, giving a total of 16 graphs per matching graph. (*A*) Average condition α-frequency band (10–13 Hz) matching graph. Lines indicate interareal interactions. Line color (minimum, black; maximum, white) and widths are proportional to the edge-matching index, M^E (M^E_{min} = 0.13, M^E_{max} = 1). For example, M^E = 0.5 indicates that the given edge is significant in half of the graphs merged into the matching graph. The graph's M^E_{min} value thus indexes the overall stability and robustness. Spheres indicate brain regions. The sphere radius is proportional to the region's degree, d (d_{max} = 56). Sphere color denotes vertex k-coreness, with the white color indicating regions belonging to the graph's maximum k-core (k_{max} = 13). Green borders encircle regions with vertex betweenness centrality values in the greatest 10th percentile. The border width is proportional to the betweenness centrality value. (*B*) Hub classification of the individual α-band average condition graphs that were used in the matching graph in *A*. The bars indicate the fraction of the graphs (x axis) in which a brain area (y axis) was classified as a hub on the basis of belonging to the top 10th percentile of degree (p_{degree}) or betweenness centrality ($p_{betweenness}$) values. The bar colors indicate whether the brain area belonged to the parietal (blue) or frontal (red) region, to the visual regions in the OC or OTC (green) region, or to other brain regions (gray). (*C*) Average condition matching graph for the β-band (18–24 Hz, M^E_{min} = 0.12, M^E_{max} = 0.81, d_{max} = 35, k_{max} = 8). (*D*) Individual graph-based hub classification in the β-band. (*E*) Average condition matching graph for the γ-band (30–40 Hz, M^E_{min} = 0.31, M^E_{max} = 0.94,

Legend continued on following page

d_{max} = 42, k_{max} = 8). (*F*) Individual graph-based hub classification in the γ-band. C, central; CA, calcarine; CI, cingulate; CN, cuneus; F, frontal; G, gyrus; IN, insula; P, parietal; S, sulcus; T, temporal; O, occipital; a, anterior; ang, angular; cal, callosal; col, collateral; i, inferior; int, intra; ist, isthmus; fus, fusiform; la, lateral; m, middle; orb, orbital; p, posterior; pa, para; pah, parahippocampal; pla, planum temporale and polare; pe, peri; pr, pre; po, post; s, superior; tr, transverse.

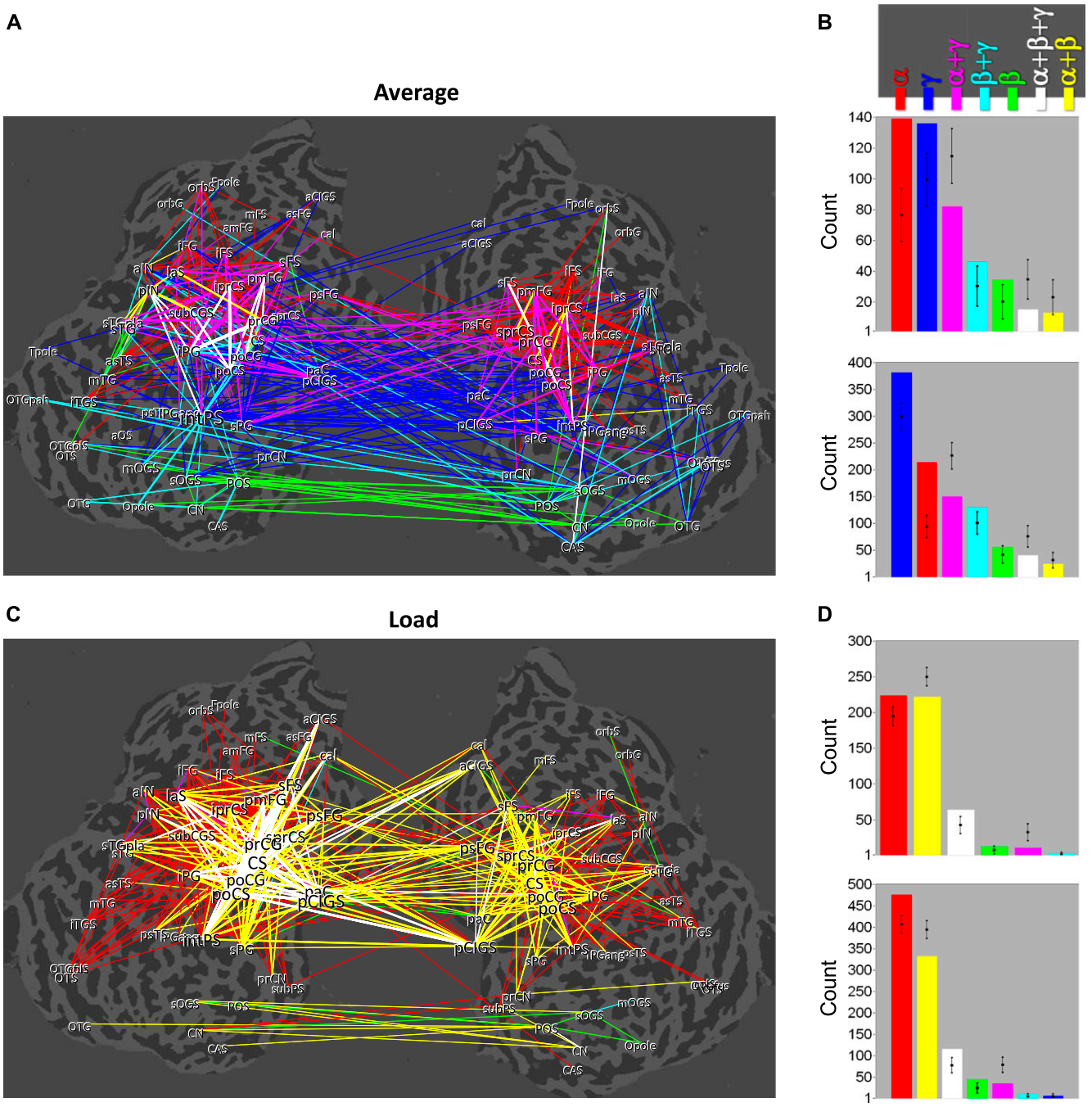

Fig. S4. Colocalization analysis of α-, β-, and γ-band networks in the average and load conditions. (*A*) Colocalization graph of α-, β-, and γ-band synchrony in the average condition. The edges of each band were allocated one of the red, green, or blue (RGB) colors (α = red, β = green, γ = blue) when they exceeded the edge-matching index (M^E_{thres} = 0.15) in the given band. Otherwise, the edges were black. The final edge colors were obtained by a direct edge-wise RGB superposition. The graph's total M^E_{min} = 0.15 corresponds to K = 0.084. The edge widths are proportional to the edge-matching index. (*B*) (*Upper*) Histogram of the edge colors in *A*. (*Lower*) Histogram of edge colors in the average condition colocalization graph at M^E_{min} = 0.1 (K = 0.173) reveals a qualitatively similar edge color distribution as M^E_{min} = 0.15 and shows that the color distribution is not strongly influenced by the threshold level. The centers of the error bars indicate the expected values of edge counts per color, which were obtained with 10^5 shufflings and resuperpositionings of the edge composite (RGB) colors. The error bars indicate the mean ± 3 SD, which corresponds to $P < 0.01$ with a Bonferroni correction by the number of possible color combinations (7). The histograms show that there are more solitary α- and γ-edges and less α-γ- and α-β-γ-edges than expected by chance, suggesting that the α- and γ-networks are partially spatially segregated. (*C*) Colocalization graph of α-, β-, and γ-band networks in the load condition. The graph was constructed as in *A*. The graph's total M^E_{min} = 0.15 corresponds to K = 0.096. (*D*) (*Upper*) Histogram of edge colors in *C*. (*Lower*) Histogram of edge colors in the load condition colocalization graph at M^E_{min} = 0.1 (K = 0.183) reveals a qualitatively similar edge color distribution as M^E_{min} = 0.15. The histograms and surrogate data were computed as in *B*. As in the average condition, there were more solitary α-edges and less α-γ-edges than expected in the load condition. However, the count of colocalized α-β-γ-edges was higher than predicted by the surrogate. These multiband interactions were robust among the left hemispheric frontoparietal regions, notably between the intPS, sprCS (i.e., putative frontal eye fields), and pmFG and sFS (i.e., putative premotor/dorsolateral prefrontal cortex). C, central; CA, calcarine; CI, cingulate; CN, cuneus; F, frontal; G, gyrus; IN, insula; P, parietal; S, sulcus; T, temporal; O, occipital; a, anterior; ang, angular; cal, callosal; col, collateral; i, inferior; int, intra; ist, isthmus; fus, fusiform; la, lateral; m, middle; orb, orbital; p, posterior; pa, para; pah, parahippocampal; pla, planum temporale and polare; pe, peri; pr, pre; po, post; s, superior; tr, transverse.

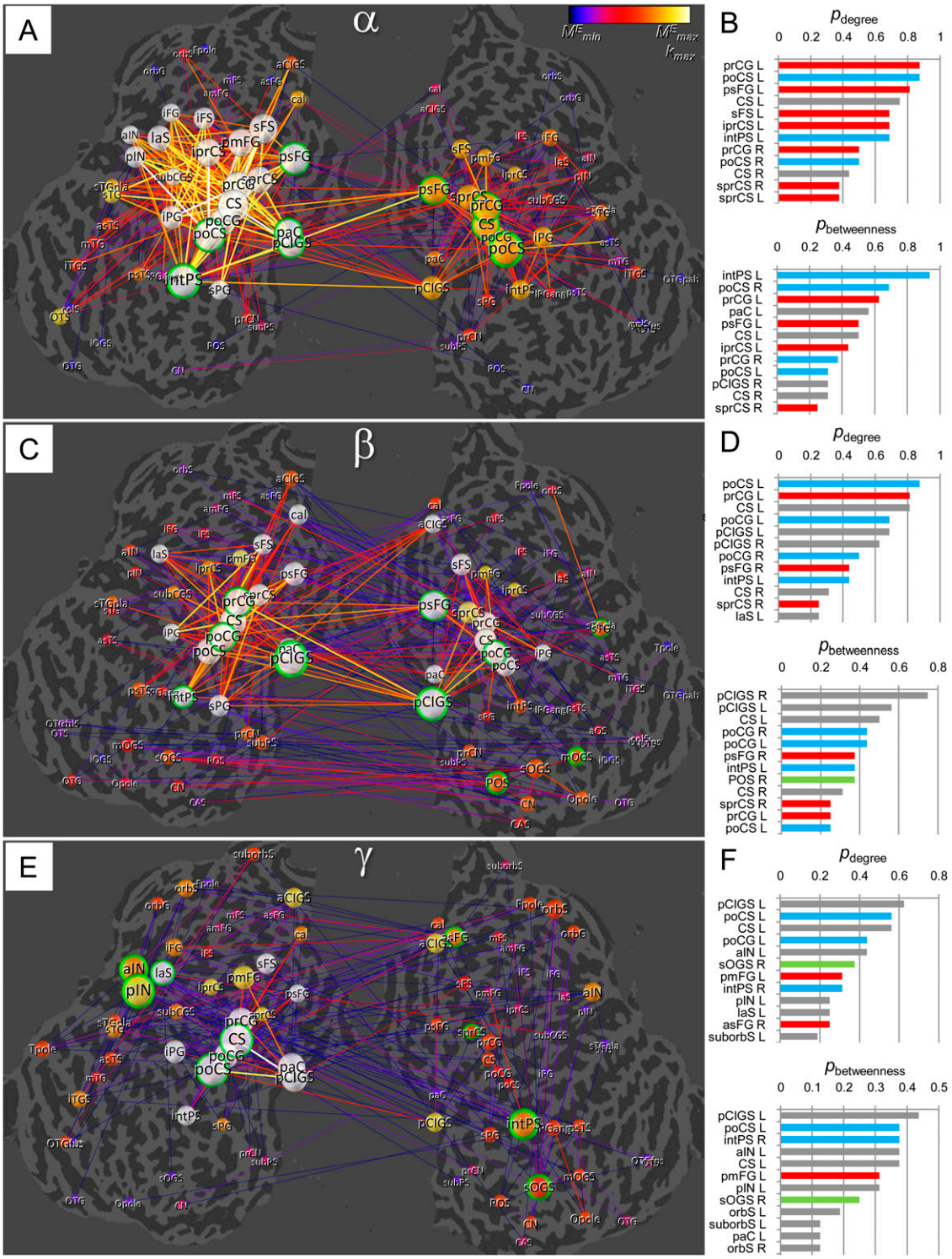

Fig. S5. Complete load condition matching graphs and hub classification for Fig. 3. (*A*) Load condition: α-band (M^E_{min} = 0.43, M^E_{max} = 1, d_{max} = 36, k_{max} = 14). (*B*) Hub classification of the individual α-band load condition graphs that were used in the matching graph in *A*. The bars and colors are as in Fig. S3. (*C*) Load condition matching graph for the β-band (M^E_{min} = 0.18, M^E_{max} = 1, d_{max} = 35, k_{max} = 11). (*D*) Individual graph-based hub classification in the β-band. (*E*) Load condition matching graph for the γ-band (M^E_{min} = 0.1, M^E_{max} = 0.69, d_{max} = 22, k_{max} = 7). (*F*) Individual graph-based hub classification in the γ-band. C, central; CA, calcarine; CI, cingulate; CN, cuneus; F, frontal; G, gyrus; IN, insula; P, parietal; S, sulcus; T, temporal; O, occipital; a, anterior; ang, angular; cal, callosal; col, collateral; i, inferior; int, intra; ist, isthmus; fus, fusiform; la, lateral; m, middle; orb, orbital; p, posterior; pa, para; pah, parahippocampal; pla, planum temporale and polare; pe, peri; pr, pre; po, post; s, superior; tr, transverse.

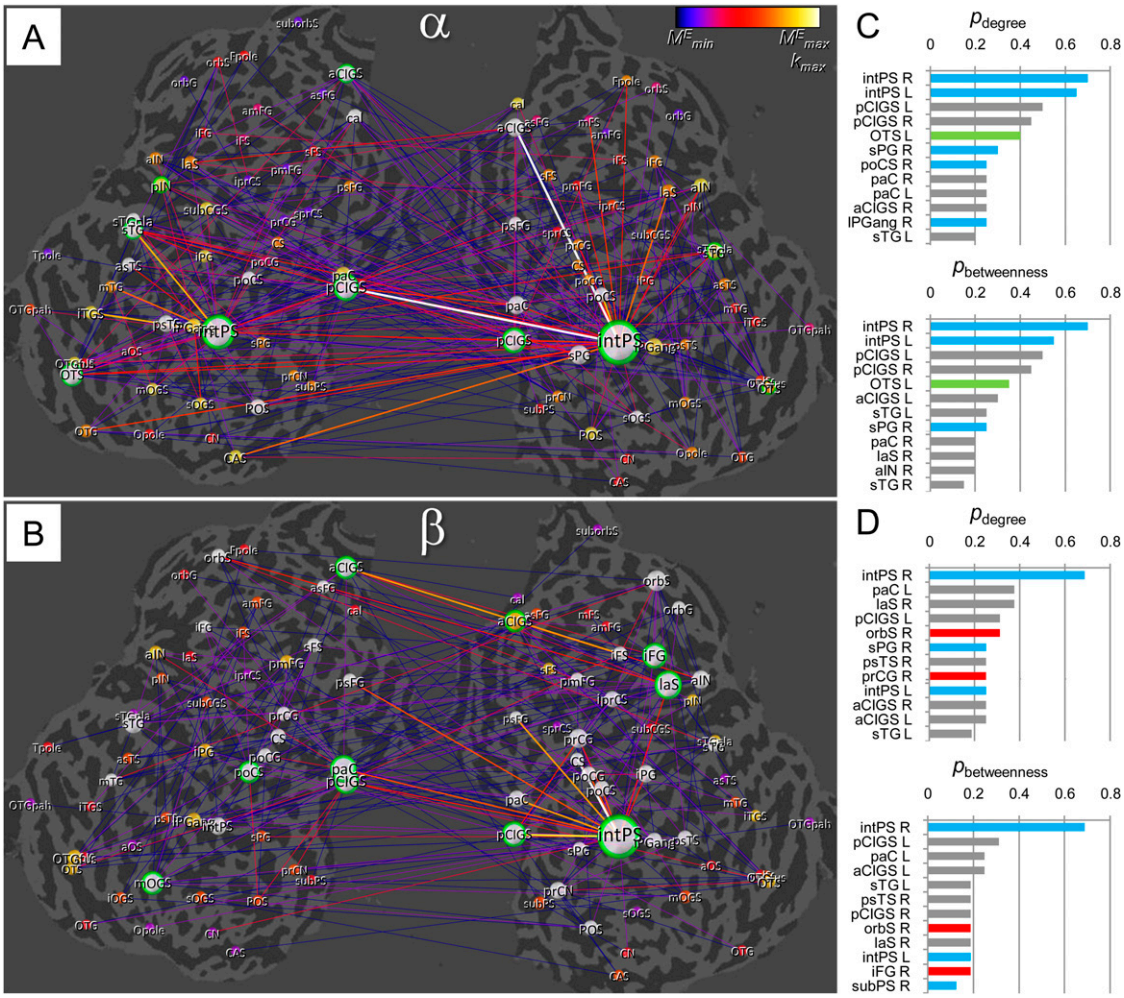

Fig. S6. Complete capacity condition matching graphs and hub classification for Fig. 4. Each matching graph was obtained from four wavelet frequencies and four retention period time windows, giving a total of 16 graphs per matching graph. (*A*) α-Frequency band (here, 9–12 Hz) matching graph (M^E_{min} = 0.24, M^E_{max} = 0.6, d_{max} = 58, k_{max} = 7). (*B*) Hub classification of the individual α-band capacity condition graphs that were used in the matching graph in *A*. The bars and colors are as in Fig. S3. (*C*) β-Frequency band (18–24 Hz) matching graph (M^E_{min} = 0.18, M^E_{max} = 0.63, d_{max} = 36, k_{max} = 5). (*D*) Individual graph-based hub classification in the β-band. C, central; CA, calcarine; CI, cingulate; CN, cuneus; F, frontal; G, gyrus; IN, insula; P, parietal; S, sulcus; T, temporal; O, occipital; a, anterior; ang, angular; cal, callosal; col, collateral; i, inferior; int, intra; ist, isthmus; fus, fusiform; la, lateral; m, middle; orb, orbital; p, posterior; pa, para; pah, parahippocampal; pla, planum temporale and polare; pe, peri; pr, pre; po, post; s, superior; tr, transverse.

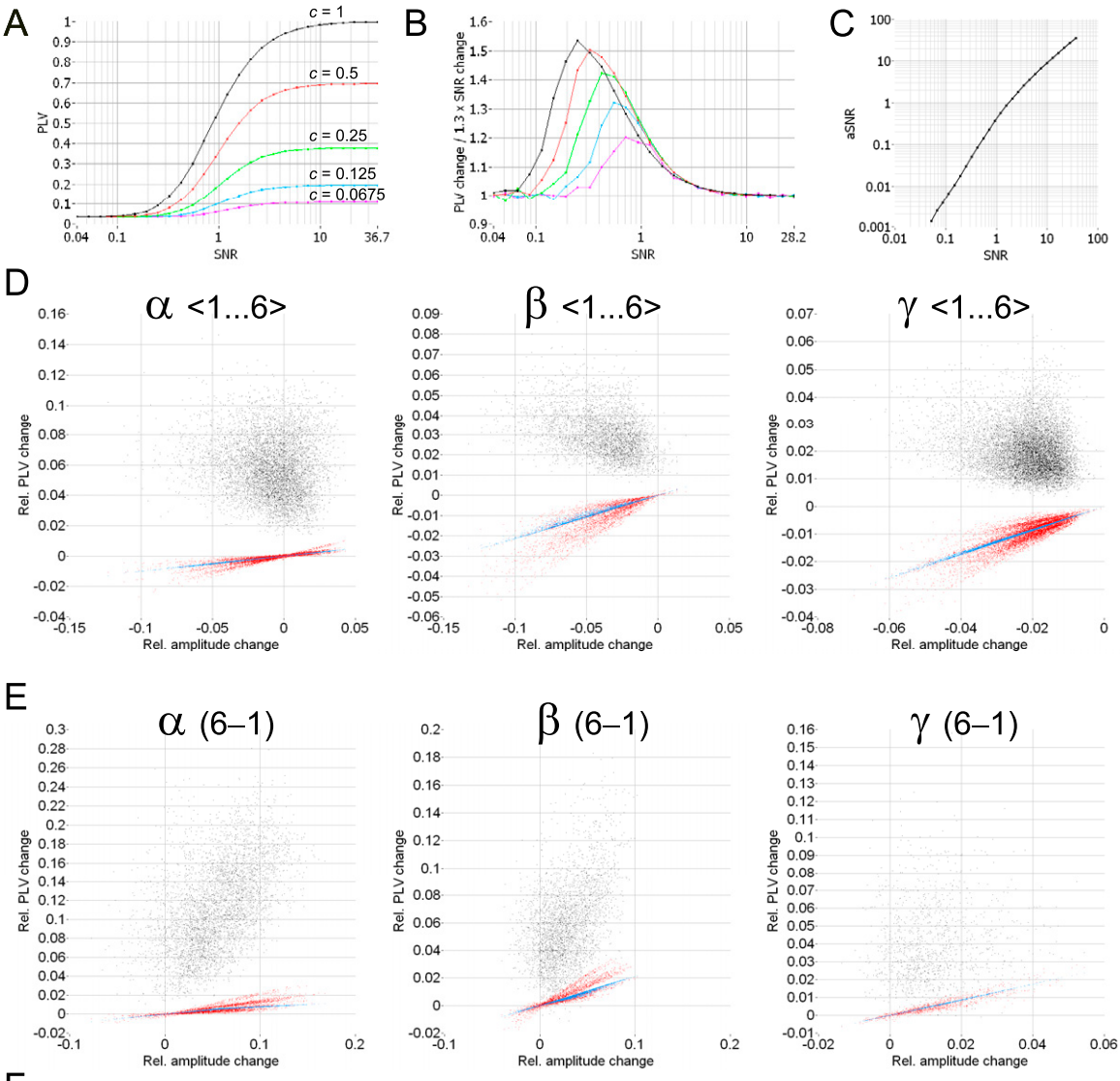

F

	α <1…6>	α (6–1)	β <1…6>	β (6–1)	γ <1…6>	γ (6–1)
aSNR	3.42	3.42	1.55	1.55	0.75	0.75
Estimated SNR	4.30	4.30	2.35	2.35	1.44	1.44
Accepted (%) *Accepted @ aSNR = 0.5 (%)*	0 *0.06*	0 *1.36*	0 *0*	0.41 *5.39*	0 *0*	1.82 *3.65*
Δ Amplitude (% +/– SD)	–0.9 +/– 2.1	5.4 +/– 3.6	–3.9 +/– 2.3	2.8 +/– 2.4	–2.1 +/– 0.8	1.2 +/– 1.0
Δ PLV (% +/– SD)	5.8 +/– 1.9	11.3 +/– 4.6	3.0 +/– 1.1	5.9 +/– 2.9	2.0 +/– 0.8	4.0 +/– 2.2
Pred. Δ PLV(% +/– SD)	–0.1 +/– 0.3	0.6 +/– 0.5	–1.0 +/– 0.8	0.7 +/– 0.7	–0.9 +/– 0.5	0.5 +/– 0.5
Linear R^2	0.015	0.237	0.134	0.197	0.035	0.007
Pred. Linear R^2	0.760	0.487	0.699	0.787	0.709	0.868

Fig. S7. Evaluation of the relation between the VWM-related amplitude and phase synchrony modulations. (*A*) *PLV* of two simulated signals as a function of their SNR. Coupling strengths of 1, 0.5, 0.25, 0.125, and 0.0675 are indicated by black, red, green, blue, and purple lines, respectively. (*B*) Relative change in *PLV* for a constant relative increase in SNR as a function of the SNR. The relative change was obtained as $(PLV_{i+1} - PLV_i)/PLV_i$, with $SNR_{i+1} = SNR_i \times 1.3$. (*C*) aSNR as a function of the (true) SNR. (*D*) Relative change in *PLV* as a function of the relative change in amplitude in the average condition. Black dots, observed *PLV* changes; red and blue dots, *PLV* changes predicted by the amplitude modulation-caused SNR changes (red, aSNR scaled according to local amplitude; blue,

Legend continued on following page

aSNR constant across the cortical surface; details provided in *SI Text*). The *PLV* and amplitude modulations were obtained by comparing the baseline and retention periods, such that the relative change in $PLV = (PLV_R - PLV_{BL})/PLV_{BL}$ and the relative change in amplitude = $(A_R - A_{BL})/A_{BL}$, where the subscripted R denotes the retention period and the subscripted BL denotes the baseline. (*E*) Relative change in *PLV* as a function of the relative change in amplitude in the six-object vs. one-object condition that was used to investigate the memory load effects on phase synchrony and amplitude modulation. Colors are as in *D*. The relative change in $PLV = (PLV_{6O} - PLV_{1O})/PLV_{1O}$ and the relative change in amplitude = $(A_{6O} - A_{1O})/A_{1O}$, where subscripted 1O and 6O denote the retention periods of one-object and six-object memory load conditions, respectively. (*F*) Summary of the numerical details. Pred., predicted; Rel., relative.

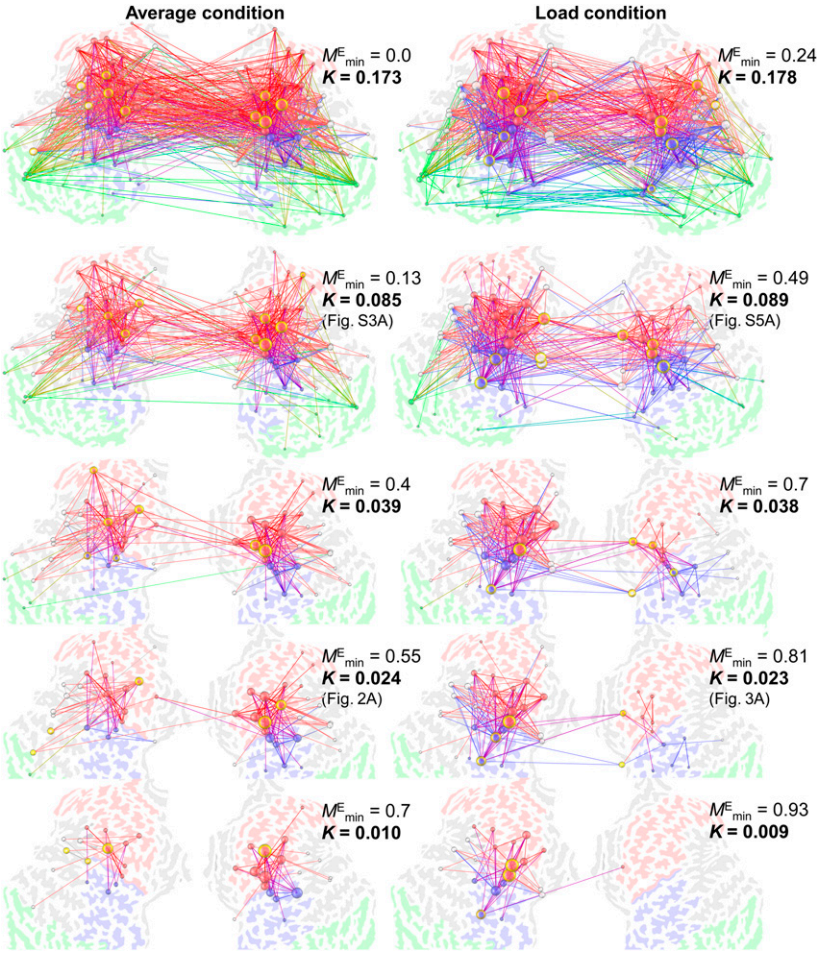

Fig. S8. Illustration of graph pruning by increasing the minimum edge-matching index (M^E_{min}). (*Left*) Column shows the average condition graph in the α-band at five M^E_{min} levels (0, 0.13, 0.4, 0.55, and 0.7), which indicates the minimum proportion of graphs from all graphs in the matching graph in which a given edge must be present (significant) to be visualized. The edge and vertex coloring, the vertex sizes and edge thicknesses, and the identification of hubs correspond to the scheme used in Figs. 2–4. At $M^E_{min} = 0$, all significant edges in any of the 16 α-band retention period graphs are visualized. At $M^E_{min} = 0.55$, all visualized edges are present in at least 55% of the graphs (i.e., in 9 of 16 graphs). The connection density, *K*, decreases with increasing M^E_{min}. The values of *K* corresponding to the visualized values of M^E_{min} are shown in the figure. (*Right*) For a pair-by-pair comparison, the load condition graphs at the same *K* levels are shown.